In Situ, Nonlinear Soil Response Applying an Active Source

Fred Pearce, M. Nafi Toksoz, F. Dale Morgan, and Paul Johnson (LANL)

Abstract

Soil sites have a profound effect on ground motion during earthquakes due to their low wave speeds, layered structure, and nonlinear constitutive relationship. Measurements of nonlinear soil response under natural conditions are critical to understanding soil behavior during earthquakes. Currently, quantitative measurements of nonlinear soil response are derived from laboratory experiments on small samples. In this paper, we extend laboratory methods for measuring nonlinear soil response to field-scale. We observe the *in situ*, nonlinear response of a natural soil formation using measurements obtained immediately adjacent to a large vibrator truck. The source generates a steady-state wavefield in the soil formation at a range of discrete source frequencies and amplitudes. Accelerometers within the source provide an estimate of the source output to the soil, and an array of 4 accelerometers adjacent to the source record the wavefield at 1.5 m spacing. We develop a homodyne analysis to extract the steady-state amplitude at each discrete source frequency and amplitude without contamination from source harmonics. Steady-state amplitude ratios are computed between the receivers and the source, and between adjacent receiver pairs within the array. Both sets of amplitude ratios show dramatic decreases in peak frequency as the source amplitude is increased. These peak frequency shifts are qualitatively similar to the nonlinear soil response observed for laboratory samples under resonance conditions. Amplitude ratios between adjacent receiver pairs suggest the nonlinear soil response persists across the receiver array and is not limited to the source-soil contact region. The magnitudes of the observed peak shifts appear to depend on their frequency, a proxy for depth, which is consistent with the confining pressure dependence of soil nonlinearity observed in laboratory experiments. Future work will include measurements of steady-state phase velocities across the array to better understand the nature of nonlinear wave propagation within natural soil formations.

1. Introduction

As many populated areas and infrastructure are located on soils, particular emphasis has been placed on predicting earthquake ground motion at soil sites. Two key factors contribute to ground motion amplification at soil sites: soil structure and nonlinear constitutive relationship. The layered structure of soil deposits often contain strong impedance contrasts, such as the soil-rock interface or the water table, which trap seismic energy near the surface. Reverberations

within the soil column can significantly amplify ground motion at one or more resonance frequencies of the soil formation [Williams et al., 2000]. When large ground motion is expected, the amplitude dependent strength of the soil formation (nonlinearity) must be included in ground motion predictions. Many observations have shown that the amplification at soil sites can shift to lower frequencies during large earthquakes compared to small earthquakes [Field et al., 1997; Field et al., 1998, Beresnev and Wen, 1996; Bonilla et al., 2005].

Quantifying the nonlinear response of natural soils is generally achieved through laboratory experiments on small soil samples (generally a few centimetres in diameter) [Hardin, 1972; Seed, 1986]. Laboratory observations on soil samples have shown that the soil microstructure begins to "soften" when dynamic strains exceed about 10^{-6} at ambient pressure conditions whereby the soil dynamic modulus and quality factor (Q) decrease in proportion to amplitude [Hardin, 1972; Johnson and Jia, 2005]. Furthermore, laboratory measurements have shown the amplitude dependence of soil modulus and Q within the large-strain regime is strongly dependent on confining pressure, grain-size, and water content [e.g., Hardin, 1972; Johnson and Jia, 2005], which can vary greatly in natural soil deposits. Currently, there is a near complete reliance on laboratory experiments to quantify the nonlinear behaviour of soils [Stokoe et al., 2001]. However laboratory experiments cannot reproduce boundary conditions representative of *in situ* conditions within a natural soil formation, particularly at the scale of seismic wavelengths.

In this paper, we describe a field-scale experiment designed to measure the nonlinear response of a natural soil formation. A large vibrator truck is used to generate a steady-state wavefield in the soil formation across a broad range of frequencies and amplitudes. We collect measurements of the source output and 3-components of ground motion within a small array immediately adjacent to the source. The same vibrator truck was used in experiments described in Lawrence et al. [2008]. In that work experiments were conducted at a different location and

the analysis was focused on measurements of surface wave phase velocities. Here we measure nonlinear soil behaviour by examining changes in steady-state amplitude ratios between receiver pairs as the source amplitude is increased. We develop a homodyne analysis to measure the steady-state amplitudes at each frequency and amplitude while removing contamination from harmonics, which can be significant for vibrator truck sources [Lebedev and Beresnev, 2004; Solodov & Beresnev, 2006]. Steady-state amplitude ratios between adjacent receiver pairs help discriminate nonlinearity of the soil formation from source and near-source effects.

We focus this study on the development of new experimental and data analysis procedures for measuring nonlinear soil response. First, we describe the site, instrumentation, and source protocol used in the experiment. Then, we present the raw data and give a description of the homodyne analysis. This is followed by the results, discussion and conclusions.

2. Experiment

2.1 Site Description

We conducted a field experiment at the Capitol Aggregates Test site near Austin, Texas where 11-m of young, unconsolidated point bar sediments overlie a soft shale (point bars are deposits formed along the inside of a river bend). The site was selected primarily because of extensive site characterization work previously conducted by Kurtulus et al. [2005]. Near-surface soils consist of predominately non-plastic silt with intermittent silty sand, based on borehole soil samples. Results from the Spectral Analysis of Surface Waves (SASW) method provided the S-wave velocity profile shown in Figure 1a [Kurtulus et al., 2005]. S-wave velocities generally increase with increasing depth, and several impedance contrasts (interfaces between layers) are present at depth (Figure 2b).
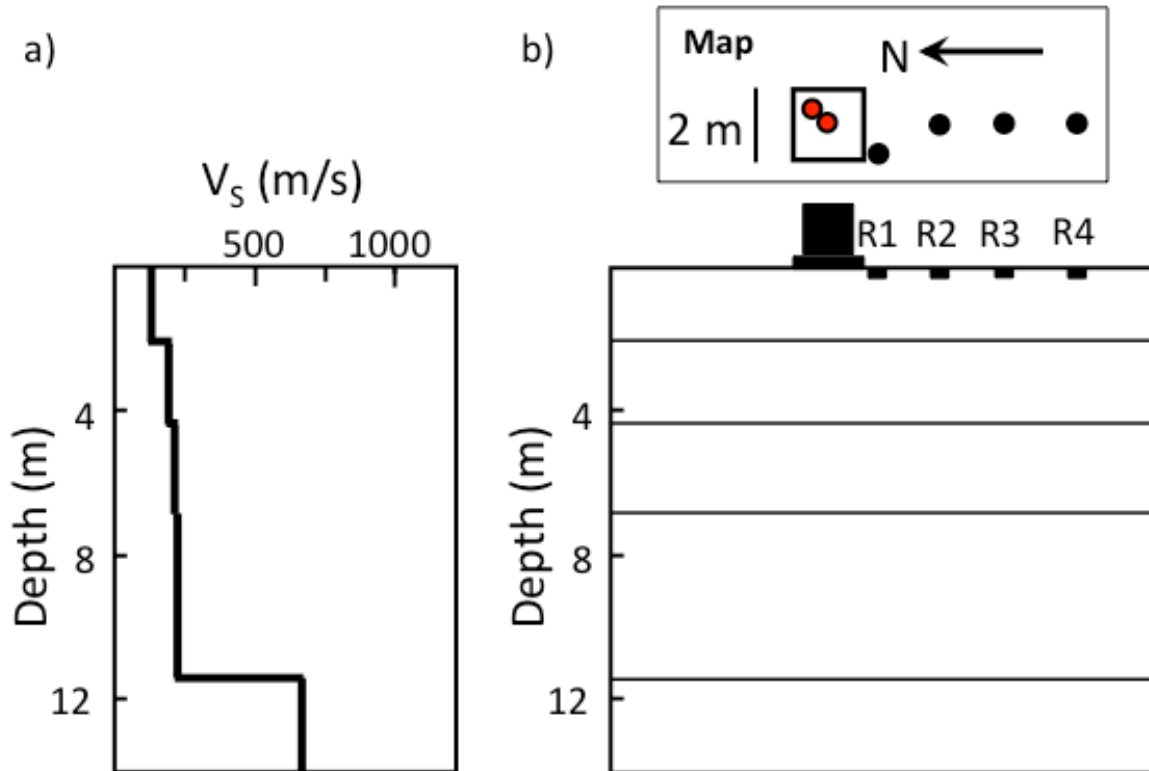
Figure 1 – a) S-wave velocity versus depth for the test site modified from Kurtulus et al. [2005] and b) The location of source and receivers at the test site. Map view and depth profile are at the same scale. Map view shows outline of base plate (black square), source accelerometers (red circles), and receiver accelerometers (solid black circles). Depth profile shows the source location (large black rectangles) and receiver pads (small black rectangles). Horizontal lines show locations of impedance contrasts at depths of 2-m, 4.5-m, 7-m (water table) and 11-m.

2.2 Instrumentation

Figure 1b shows the location of the source and receivers at the test site. The source is a large vibrator truck, 'T-Rex', developed and maintained by the Network for Earthquake Engineering Simulation Program of the National Science Foundation [Stokoe et al., 2004]. The source has a maximum vertical force output of approximately 267 kN (27.2 metric tons) and couples to the ground via a 2x2 m plate. A function generator controls the frequency and amplitude of the source. Two accelerometers built into the source estimate the force output delivered to the ground. The function generator input to the source (S^{in}) and the corresponding force output delivered by the source to the ground surface (S^{out}) are recorded for analysis. The

raw recordings of S^{in} and S^{out} are in units of voltage, which we converted to units of acceleration (m/s/s) using calibration parameters provided by the truck operator. While the source can shake either vertically or horizontally, we only consider vertical shaking in this experiment.

The near-source wavefield was recorded using four receivers, R1-R4, with increasing distance from the source as shown in Figure 1b. The array extends along a N-S line from the source and was placed as close as possible to the source to record the largest amplitudes of ground motion. The receivers were Kinemetrics three-component accelerometers (K2) designed for large accelerations (> 2g). Each receiver was anchored to a concrete pad with diameter of approximately 0.35 m (much smaller than wavelengths). The concrete density was designed to match the soil density and each pad was of equal dimension within a few centimeters. The accelerometers have a flat response in the frequency band of interest; however, we converted each receiver recording from counts to units of acceleration (m/s/s) using calibration constants provided by the manufacturer.

2.3 Source Protocol

We use a source protocol developed to measure the nonlinear response of materials in the laboratory termed Nonlinear Resonance Ultrasound Spectroscopy (NRUS) [Johnson et al., 1996]. First, the source is stepped through many discrete frequencies while the input voltage to the source is held constant at its lowest level. In this experiment, the source follows a step-sweep with M=201 discrete frequencies beginning at 50-Hz (f_1) and decreasing with frequency step-size of 0.2-Hz (df):

$$f_m = f_1 - (m-1)*\Delta f, \quad m = 1, \ldots, M \quad [1].$$

The step-sweep decreases in frequency as a function of time to a minimum frequency $f_{201} = 10$Hz. The source was held at each frequency for 40 cycles so that the source shakes longer at low

frequencies than high frequencies. This assures steady-state conditions are reached at each

discrete frequency in the step-sweep.

The step-sweep is repeated for a total of N=11 source input voltages beginning with an

input voltage of 0.2-V (A_1) and a step-size of 0.2-V (ΔA) as follows:

$$A_n = A_1 - (n-1) * \Delta A, \quad n = 1, \ldots, N \quad [2].$$

Based on this source protocol, we obtain 11 step-sweep time signals for the source and receivers.

Every step-sweep time signal records a steady-state wavefield at each source frequency f_m.

3. Data

In this section we present examples of the step-sweep time signals recorded for the source

and receivers during the experiment. All recorded step-sweep time signals (source and receivers)

have a time sampling, Δt, of 0.005 sec. Figure 3 shows a comparison of step-sweeps at several

values of input voltage (A_n) for the source input (Fig. 2a) and source output (Fig. 2b). We show

only every other input voltage to highlight the structure of the time signals (the step-sweep time

signals not shown are very similar to those for adjacent input voltages). Each source input step-

sweep maintains constant amplitude across the entire step-sweep band (f_m) as expected for the

function generator. The source output shows significant variation across the step-sweep band,

particularly at low frequencies (large step-sweep times). At small input voltages, the source

output amplitude decreases as the source frequency decreases (step-sweep time increases). At

large input voltages, the source output shows some variation across the step-sweep band but is

relatively constant. The digitizer clipped the source output time signal at the largest input voltage

(A_{11}) for over half the step-sweep frequency band. While the clipping was undesirable from a

data quality standpoint, it did allow us to verify the instrument calibration constants provided by the source operator.

The step-sweep time signals for the Z, N-S, and E-W components of each receiver are shown in Figures 4-6. We observe a clear difference between the receiver step-sweep time signals and the step-sweep time signals for the source output in Figure 3. For a given input voltage, the receiver step-sweep time signals have smaller peak amplitudes than those for the source output. All receiver components have more pronounced peaks in amplitude as compared to the source output. The Z and N-S components share similar variations in amplitude as a function of source frequency (step-sweep time), input voltage, and distance from the source. Conversely, the E-W components have the smallest amplitudes and show different variations in amplitude as compared to the Z and N-S components. The E-W component of R1 is different than the other E-W components due to its proximity to the corner of the source plate. In general, the vertical and radial components share similar characteristics; therefore, we focus the remainder of the analysis on the Z and N-S components of each receiver.

The complex nature of the source complicates the interpretation of nonlinear soil response from direct observations of peaks within the step-sweep time signals. Vibrator trucks are well known to generate significant harmonic amplitudes, particularly at their low-frequency limit where coupling becomes inefficient [Solodov & Beresnev, 2006]. Filtering each step-sweep time signal to include only frequency components within the step-sweep band (10 Hz – 50 Hz) will not eliminate harmonic contamination of the amplitudes because every source frequency at or below 25 Hz produces at least one harmonic within the step-sweep band. Therefore, we develop a more elaborate analysis technique to obtain the steady-state amplitude for each fundamental frequency in the step-sweep.
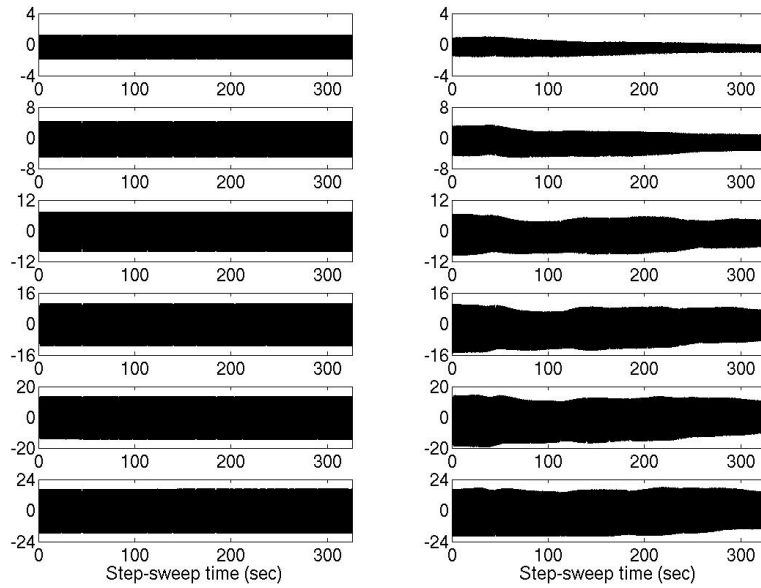
Figure 3 – Step-sweep time signals for the source input (left panels) and source output (right panels). Top panel corresponds to the lowest input voltage to the source (A_1) with successive lower panels corresponding to input voltages of A_3, A_5, A_7, A_9, and A_{11}, respectively. The x-axis of each panel is the step-sweep time in seconds. The y-axes of all panels are in units of m/s/s and the range in y-axis values increases with increasing input voltage as labeled.
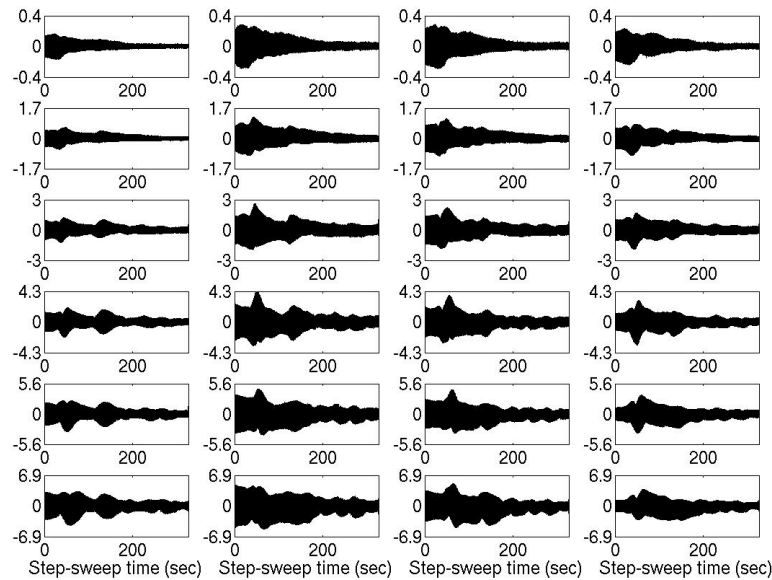

Figure 4 – Z (vertical) components of receivers: R1 (left-most panels) with R2, R3, and R4 moving from left to right. Top panels show the lowest input voltage (A_1) with successive lower panels corresponding to input voltages of A_3, A_5, A_7, A_9, and A_{11}, respectively. The x-axis of each panel is the step-sweep time in seconds. The y-axes have units of m/s/s and the labels denote range in y-axis values. Each step-sweep time signal has its mean value removed.
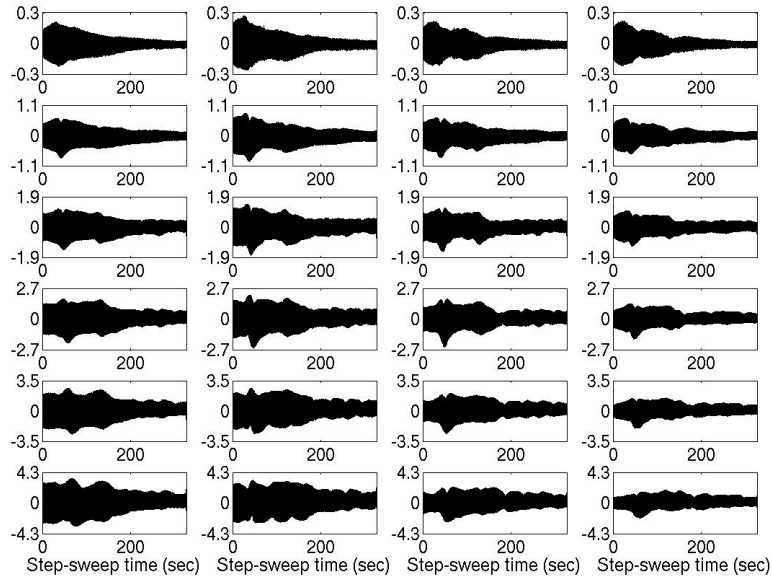
Figure 5 – N-S (radial) components of receivers: R1 (left-most panels) with R2, R3, and R4 moving from left to right. Top panels show the lowest input voltage (A_1) with successive lower panels corresponding to input voltages of A_3, A_5, A_7, A_9, and A_{11}, respectively. The x-axis of each panel is the same as Figure 4. The y-axes have units of m/s/s and the labels denote range in y-axis values. Each step-sweep time signal has its mean value removed.
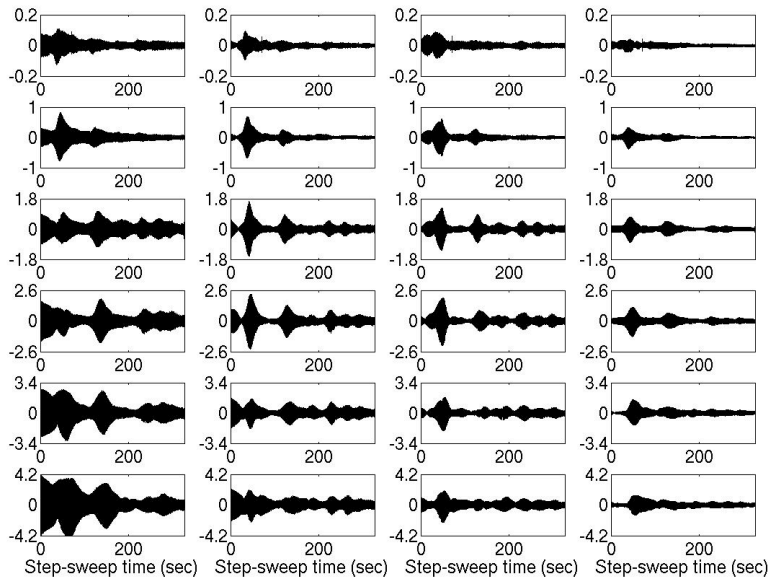

Figure 6 – E-W (transverse) components of receivers: R1 (left-most panels) with R2, R3, and R4 moving from left to right. Top panels show the lowest input voltage (A_1) with successive lower panels corresponding to input voltages of A_3, A_5, A_7, A_9, and A_{11}, respectively. The x-axis of each panel is the same as Figure 4. The y-axes have units of m/s/s and the labels denote range in y-axis values. Each step-sweep time signal has its mean value removed.

4. Homodyne Analysis

In this section, we describe the homodyne analysis used to extract the steady-state amplitude at every source frequency within a step-sweep time signal. Homodyne processing is common in many different areas of electronics, physics and acoustics where it is used to amplify a single frequency component within noisy signals (such as in a lock-in amplifier). We develop a discrete version of the homodyne to separate the steady-state amplitude at each source frequency within a step-sweep time signal from the unwanted harmonic amplitudes generated by the source.

We describe the homodyne analysis as it applies to a step-sweep time signal, $X(t_i)$, where the subscript i refers to each time sample. The first step in the homodyne analysis is to define a time window vector, $\mathbf{x}_w$, which contains a subset of J time samples from the wth window location within $X(t_i)$

$$\mathbf{x}_w = X(t_j) \quad \text{for } j = w, ..., w + J \quad [3].$$

Note that the time window vector slides across the step-sweep time signal with each $\mathbf{x}_w$ beginning at a time value of t_w within $X(t_i)$. The duration of each time window vector, T, is constant

$$T = (J - 1) * \Delta t \quad [4].$$

In general, T should be smaller than the time spent at the largest source frequency (in this experiment $40/f_1$) so that the time window vectors can resolve each discrete frequency step.

Next, a discrete homodyne is applied to every $\mathbf{x}_w$ to measure its amplitude at each source frequency, f_m. We construct a pair of orthonormal basis vectors for every f_m

$$\mathbf{I}_m = \cos(2\pi f_m t_j) \text{ for } j = 1, ..., J \quad [5]$$

$$\mathbf{Q}_m = \sin(2\pi f_m t_j) \text{ for } j = 1, ..., J \quad [6]$$

with each basis vector having J time samples (the same as $\mathbf{x}_w$). We use the Gram-Schmidt

process to make each basis vector pair orthonormal such that $\mathbf{I}_m$ and $\mathbf{Q}_m$ satisfy the following

conditions: $\mathbf{I}_m \bullet \mathbf{Q}_m = 0$, $\mathbf{I}_m \bullet \mathbf{I}_m = 1$, $\mathbf{Q}_m \bullet \mathbf{Q}_m = 1$ with $\bullet$ denoting the inner product. Then, we

project each basis vector pair onto $\mathbf{x}_w$ to measure its RMS amplitude at each f_m as follows:

$$RMS_{m,w} = \sqrt{\left(\frac{2}{J}\right)\left[(\mathbf{x}_w \bullet \mathbf{I}_m)^2 + (\mathbf{x}_w \bullet \mathbf{Q}_m)^2\right]} \quad [7].$$

In summary, the homodyne analysis takes in a step-sweep time signal and produces a 2D matrix

of amplitudes ($RMS_{m,w}$): each column refers to the source frequency, f_m, of the discrete homodyne

and each row refers to the location of the time window vector, t_w, within $X(t_i)$.

We apply the homodyne analysis to each step-sweep time signal recorded during the

experiment. In all cases, we use T equal to 0.8 sec and apply a 0.05 sec cosine taper to each side

of the time window vectors, $\mathbf{x}_w$. Figure 7 shows the amplitudes from the homodyne analysis

($RMS_{m,w}$) for S^{in}, S^{out}, and the Z component of R2 using step-sweep time signals at the lowest

input voltage (A_1). For S^{in}, $RMS_{m,w}$ has only one set of peaks with constant amplitude that follow

the exact source protocol described in section 2.3, as expected for the function generator.

However, the $RMS_{m,w}$ for S^{out} and R2 are significantly more complex than that observed for S^{in}.

The three additional sets of peaks in the $RMS_{m,w}$ of S^{out} and R2 correspond to higher harmonics of

the source frequency ($2*f_m$, $3*f_m$, and $4*f_m$). For example, when the source is shaking at 10 Hz

(f_{201}) the last time window vectors of S^{out} and R2 show significant amplitudes at 20 Hz, 30 Hz,

and 40 Hz. By applying the homodyne analysis to small windows of the step-sweep time signal,

we only follow the source protocol without contamination from the source harmonics.

The final step in the homodyne analysis is to measure a (quasi) steady-state amplitude for every source frequency in the step-sweep by tracking the peak in each $RMS_{m,w}$ that corresponds to the source protocol. For example, at the first source frequency (f_1), we locate the time window vector within $RMS_{1,w}$ where the amplitude stabilizes, which occurs at the time window location t_w = t_{peak}. The define the window vector at steady-state with an index value *peak* such that the steady-state amplitude at f_1 is

$$SAS_1 = RMS_{1,peak} \qquad [8].$$

By repeating this process for every f_m, the homodyne analysis produces a steady-state amplitude spectrum (**SAS**) from a single step-sweep. In essence, the **SAS** characterizes the steady-state response at a given input voltage to the source. Recall from the source protocol that we generate 11 different step-sweep time signals, one for each input voltage of the source, A_n. Therefore, the final output of the homodyne analysis is a set of 11 steady-state amplitude spectra, **SAS**$_n$. In the following section, we describe how the **SAS**$_n$ for the source and receivers are used to measure the nonlinear response of the soil formation.
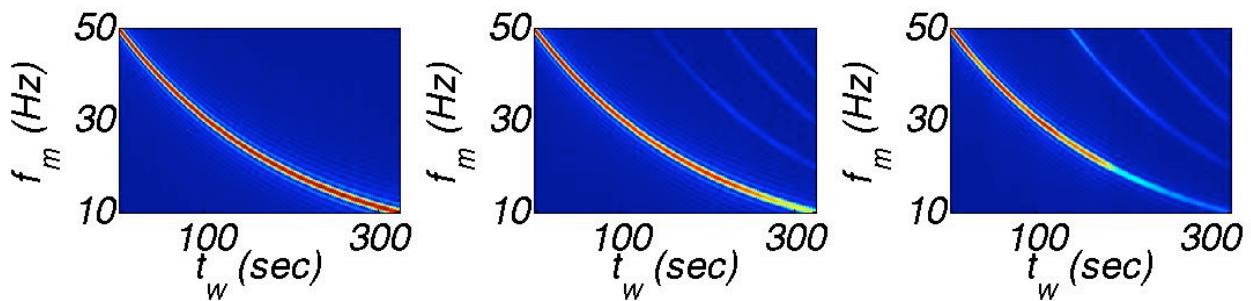

Figure 7 – Homodyne analysis output, $RMS_{m,w}$, for S^{in} (left), S^{out} (center), and the Z component of R2 (right) at the lowest input voltage (A_1). The x-axis of each panel is the location of the time window vector and the y-axis of each panel is the source frequency of the discrete homodyne as described in the text. Each $RMS_{m,w}$ is normalized by its maximum value and has a scale that ranges from 0 (blue) to 1 (red).

5. Results

In this section, we use the steady-state amplitude spectra to observe the nonlinear response of the source-soil system. First, we show the source response as characterized by the $\mathbf{SAS}_n$ for the function generator input to the source (S^{in}) and the force output exerted by the source (S^{out}). Then, we show receiver responses as described by the $\mathbf{SAS}_n$ for the Z and N-S components of each receiver. Finally, we compute the soil response using two types of steady-state amplitude ratios to isolate the *in situ*, nonlinear response of the soil formation.

5.1 Source Response

Figure 8 shows the steady-state amplitude spectra at each input voltage, $\mathbf{SAS}_n$, for S^{in} and S^{out}. Each $\mathbf{SAS}$ for S^{in} is constant across all f_m. For all A_n, the $\mathbf{SAS}$ for S^{out} increase as f_m increases. At large A_n, the $\mathbf{SAS}$ for S^{out} show significant variability at large f_m and fall off very rapidly below about 18 Hz. At small A_n, the $\mathbf{SAS}$ for S^{out} are smaller than the $\mathbf{SAS}$ for S^{in} across all f_m. At large A_n, the $\mathbf{SAS}$ for S^{out} are larger than the $\mathbf{SAS}$ for S^{in} above about 30 Hz. While S^{in} follows the source protocol, S^{out} has significant variations that depend on f_m and A_n.
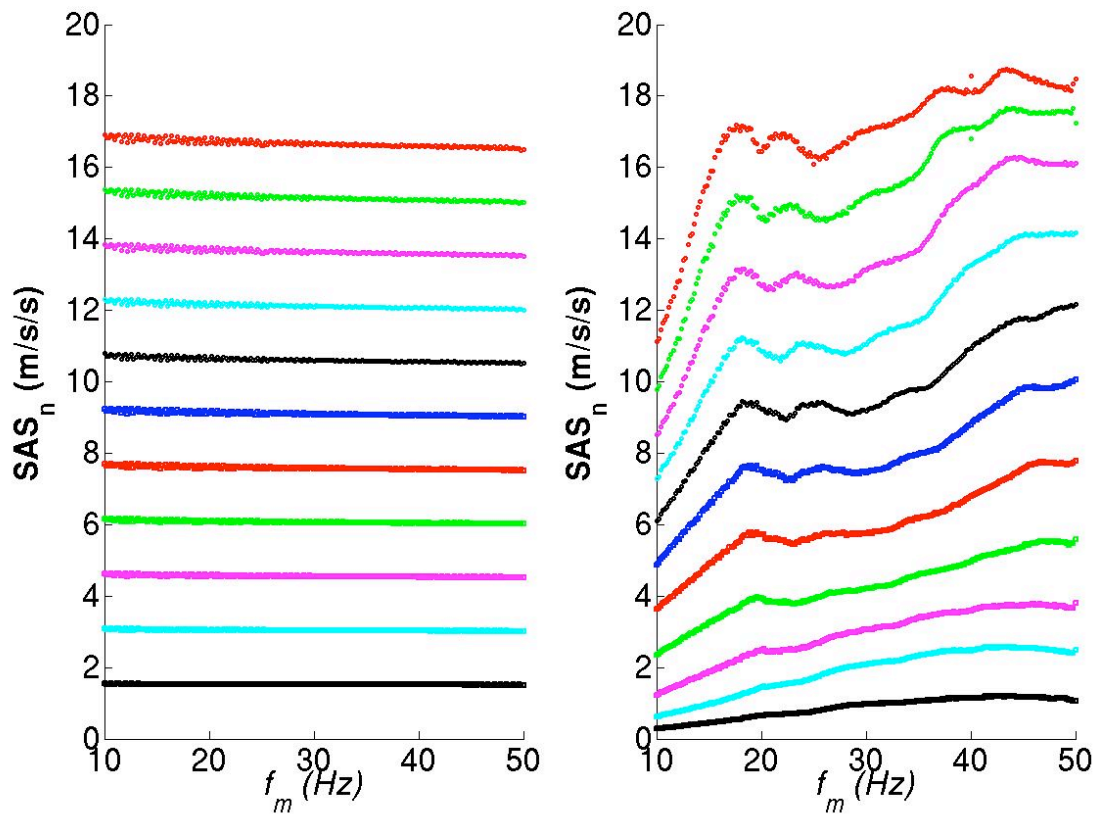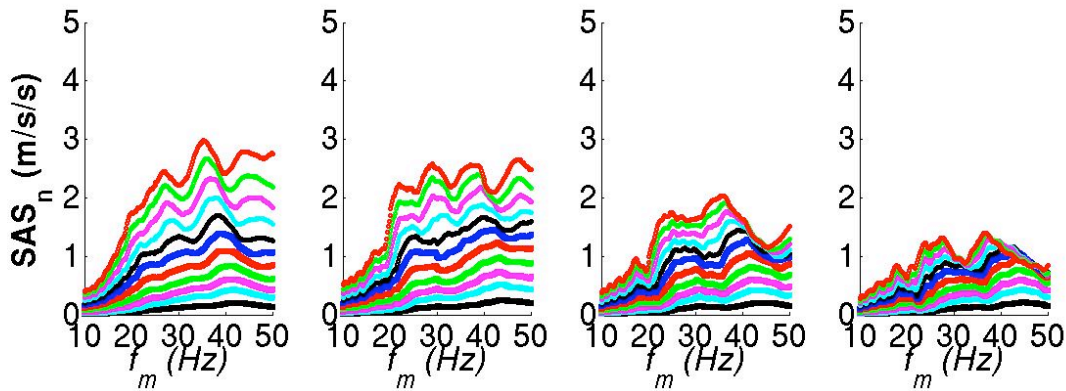
Figure 8 – Steady-state amplitude spectra at each input source voltage, $\mathbf{SAS}_n$, for S^{in} (left) and S^{out} (right). Each spectrum is color-coded with A_1 having the lowest amplitudes (black squares at the bottom) and A_{11} having the highest amplitudes (red circles at the top).

5.2 Receiver Response

Figure 9 shows the steady-state amplitude spectra at each input voltage, $\mathbf{SAS}_n$, for the Z component and N-S component of each receiver. In general, the $\mathbf{SAS}_n$ for the receiver components are much smaller in amplitude than the $\mathbf{SAS}_n$ for S^{out}. At the lowest input voltage, the $\mathbf{SAS}_n$ for the receiver components are similar in structure at all receivers. However, at larger input voltages, the $\mathbf{SAS}_n$ are more complex and vary depending on receiver location and component. Peaks are observed in the $\mathbf{SAS}_n$ for the receivers, which become more distinct at further distances from the source. The peaks in the $\mathbf{SAS}_n$ for the receivers occur at lower frequencies as the source

input voltage increases. However, we cannot interpret the soil response directly from the **SAS**$_n$ for the receivers due to variations in source output.
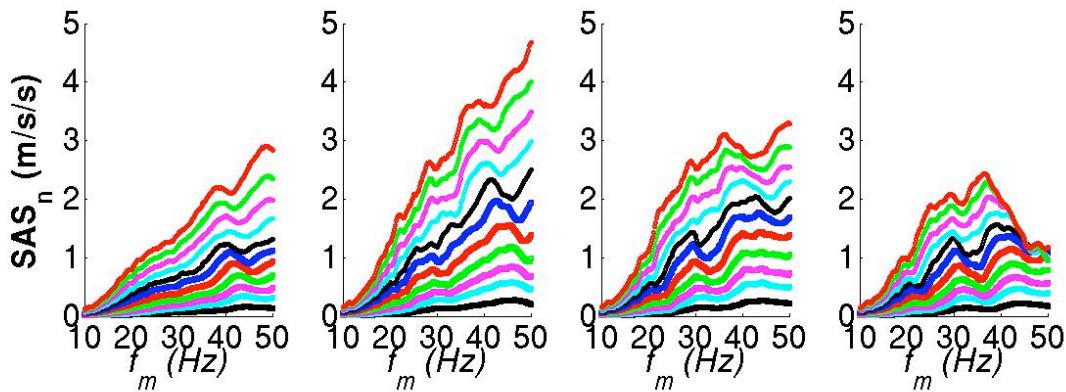
a)

b)

Figure 9 – Steady-state amplitude spectra at each input source voltage, **SAS**$_n$, for a) the Z component and b) N-S components of receivers R1, R2, R3, and R4 (from left to right). Color scheme is the same as Figure 8.

5.3 Soil Response

We compute steady-state amplitude ratios to observe the soil response during the experiment, and to distinguish pervasive nonlinearity in the soil formation from localized nonlinearity at the source-ground contact. As previously noted, amplitude ratios are commonly used to characterize nonlinear behavior in earthquake observations [Field et al., 1997]. The use of

amplitude ratios to characterize nonlinear systems relies on a first order perturbation of the linear elastic constitutive equations. This approximation is valid as long as incremental increases in source input voltage (ΔA) only produce small changes in the steady-state amplitude ratios. In other words, we must be able to correlate peaks in the steady-state amplitude spectra between adjacent source input voltages (i.e. $\mathbf{SAS}_n$ to $\mathbf{SAS}_{n+1}$). If the $\mathbf{SAS}$ vary wildly between adjacent source input voltages, then we cannot observe systematic decreases in peak frequency as an indicator of nonlinear soil response.

In addition, deriving $\mathbf{SAS}$ from only the fundamental source frequency (i.e. not including the harmonics into the homodyne analysis) to characterize the nonlinear response ignores the coupling between frequencies inherent within nonlinear constitutive relationships. For example, neglecting the coupling between frequencies will affect the amplitude of the $\mathbf{SAS}$, producing apparent attenuation because energy may be lost to other frequency components (e.g. higher harmonics). However, an apparent attenuation of the $\mathbf{SAS}$ should not be problematic as long as we can still identify the peaks in the steady-state amplitude ratios between adjacent input voltages.

Two types of steady-state amplitude ratios are computed to observe the response of the soil formation. First, we present the Receiver/Source amplitude ratios. Then, we present the Receiver/Receiver amplitude ratios. Each type of amplitude ratio is described in the following sections.

5.3.1 Receiver/Source. We divide the receiver amplitude spectra, $\mathbf{SAS}_n(R)$, by the source output amplitude spectra, $\mathbf{SAS}_n(S^{out})$, to compute the Receiver/Source amplitude ratios, $\mathbf{G}_n(R;S^{out})$,

$$\mathbf{G}_n(R;S^{out}) = \frac{\mathbf{SAS}_n(R)}{\mathbf{SAS}_n(S^{out})} \qquad [9].$$

By removing the imprint of variable source output, peaks in the Receiver/Source amplitude ratios are due to the soil response between the source and each receiver. A similar approach is typically used in the laboratory to derive the resonance modes of a sample with finite-dimensions [Guyer & Johnson, 1998].

Figure 10 and Figure 11 show the $\mathbf{G}_n(R;S^{out})$ for the Z and N-S components, respectively. As the source input voltage increases, we observe a smooth change in the structure of the Receiver/Source amplitude ratios. In general, the peak amplitudes of the $\mathbf{G}_n(R;S^{out})$ for both components decrease to lower frequency as the source input voltage increases. The peaks with the largest amplitudes (between 40-Hz to 50-Hz at the lowest source amplitude) decrease in frequency by as much as 35% as highlighted in Figure 8. Although the peaks are broad, the Receiver/Source amplitude ratios show a clear dependence on source amplitude indicative of nonlinear soil response.

However, the source-soil contact region most likely dominates the nonlinear soil response of the Receiver/Source amplitude ratios. In general, the receiver amplitudes are much smaller than the source output amplitudes as indicated by the peak values of the $\mathbf{G}_n(R;S^{out})$, which range from 15-25% for all receiver components. This suggests a large amount of energy does not make it from the source-soil contact to the receiver array. This apparent attenuation is much larger for all receiver components below about 20 Hz presumably due to less efficient coupling and increased harmonic generation.
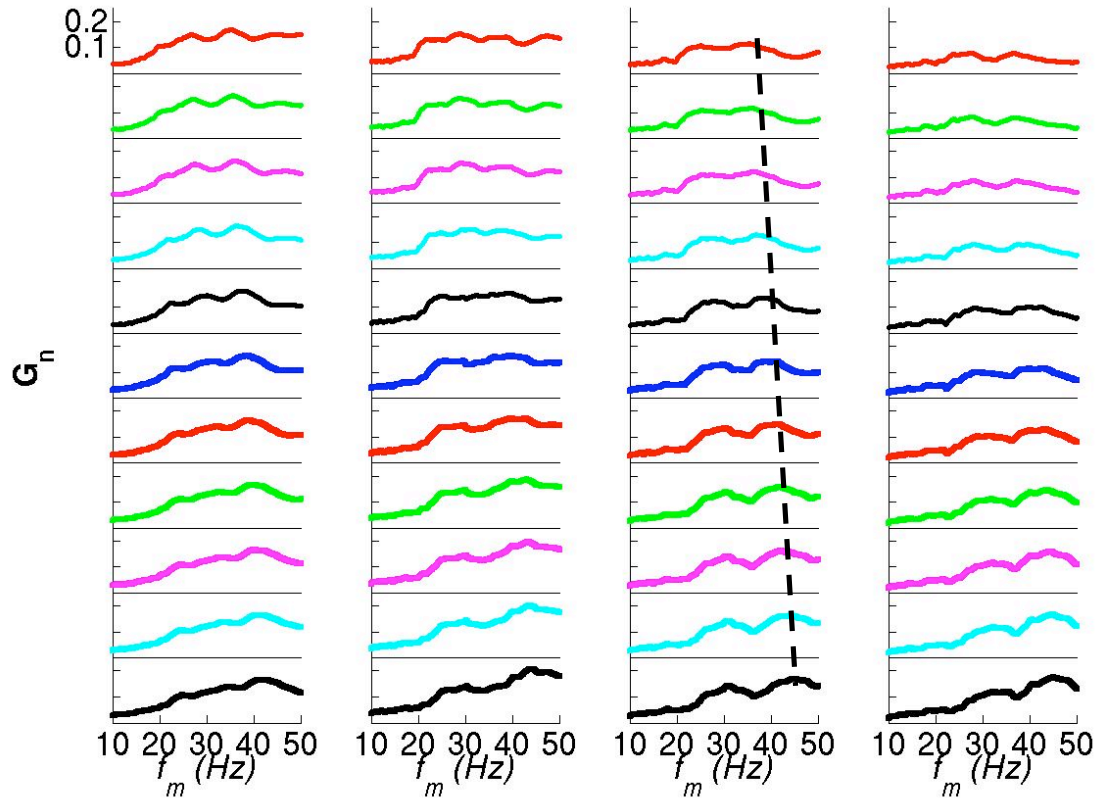
Figure 10 – Receiver/Source amplitude ratios, $\mathbf{G}_n(R;S^{out})$ for the Z component of receivers R1-R4 are shown from left to right, respectively. The input voltage increases upwards with the bottom panels showing the amplitude ratios at the lowest input voltage (black) and the top panels showing the amplitude ratios at the highest input voltage (red). The y-axis tick marks are at 0.1 and 0.2 as shown in the upper left corner and they are the same for each panel. Dashed black line highlights the shift in peak frequency for R3.
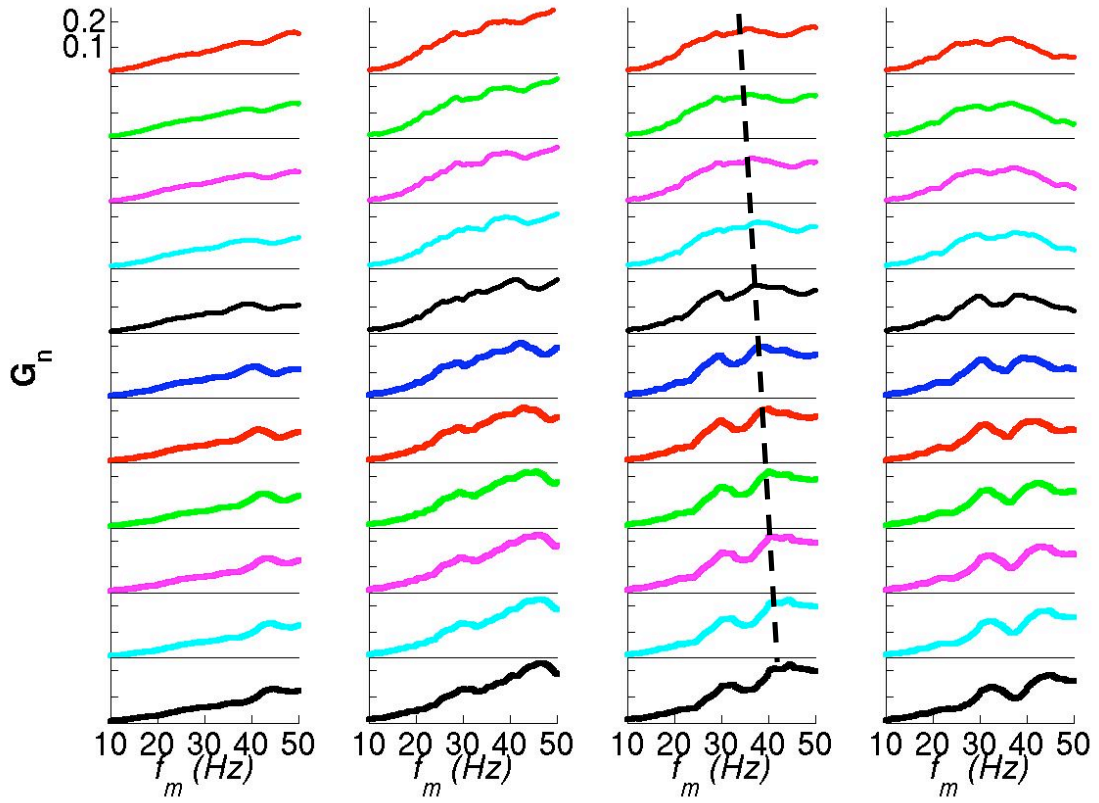
Figure 11 – Receiver/Source amplitude ratios, $\mathbf{G}_n(R;S^{out})$ for the N-S component of receivers R1-R4 are shown from left to right, respectively. The panels are arranged identical to Figure 10. Dashed black line highlights the shift in peak frequency for R3.
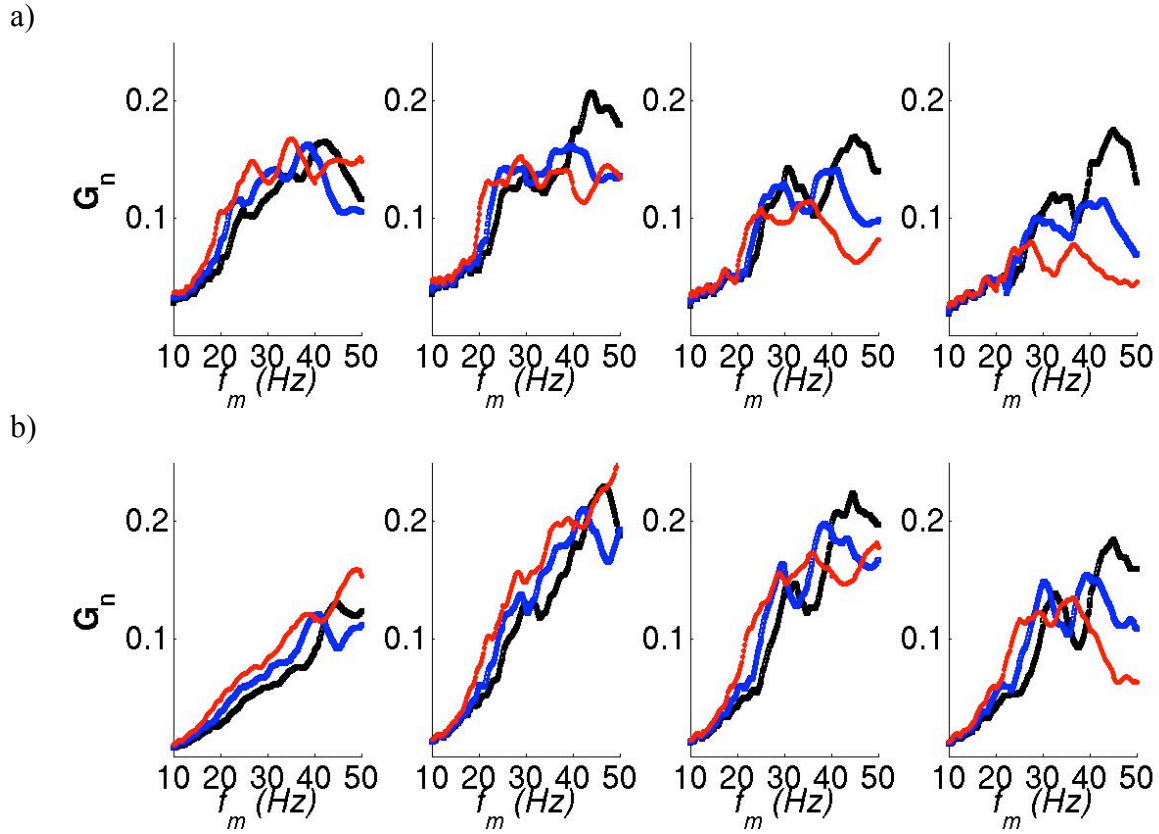
a)

b)

Figure 13 – Receiver/Source amplitude ratios for A_1 (black), A_6 (blue), and A_{11} (red). a) Z components and b) N-S components of receivers R1-R4 are shown from left to right, respectively.

5.3.2 Receiver/Receiver. We divide the amplitude spectra from a receiver farther from the source, $\mathbf{SAS}_n(R[X+1])$, by the amplitude spectra from a receiver closer to the source, $\mathbf{SAS}_n(R[X])$, to compute the Receiver/Receiver amplitude ratios, $\mathbf{G}_n(R[X+1];R[X])$,

$$\mathbf{G}_n(R[X+1];R[X]) = \frac{\mathbf{SAS}_n(R[X+1])}{\mathbf{SAS}_n(R[X])} \qquad [10]$$

where X refers to the receiver pair being analyzed. For example, when X=1 we divide the amplitude spectra of R2 by the amplitude spectra of R1.

Figure 14 and Figure 15 show the $\mathbf{G}_n(R[X+1]; R[X])$ for the Z and N-S components, respectively. The Receiver/Receiver amplitude ratios show a similar decrease in peak frequency as

the input voltage increases for both components. The changes in the Receiver/Receiver amplitude

ratios as a function of input voltage are dramatic for high frequencies, but much smaller for

frequencies below 20 Hz as highlighted in Figure 16. We do not observe the falloff at low

frequencies observed for the Receiver/Source amplitude ratios. The Receiver/Receiver amplitude

ratios are generally above 1.0 at the lowest input voltages. At large input voltages, the

Receiver/Receiver amplitude ratios are generally at or below 1.0 and tend to falloff as the source

frequency increases. We note that the anomalously high values of the $G_n(R2;R1)$ are a result of

R1 being close to the corner of the source plate so it's N-S amplitude spectra are relatively small.
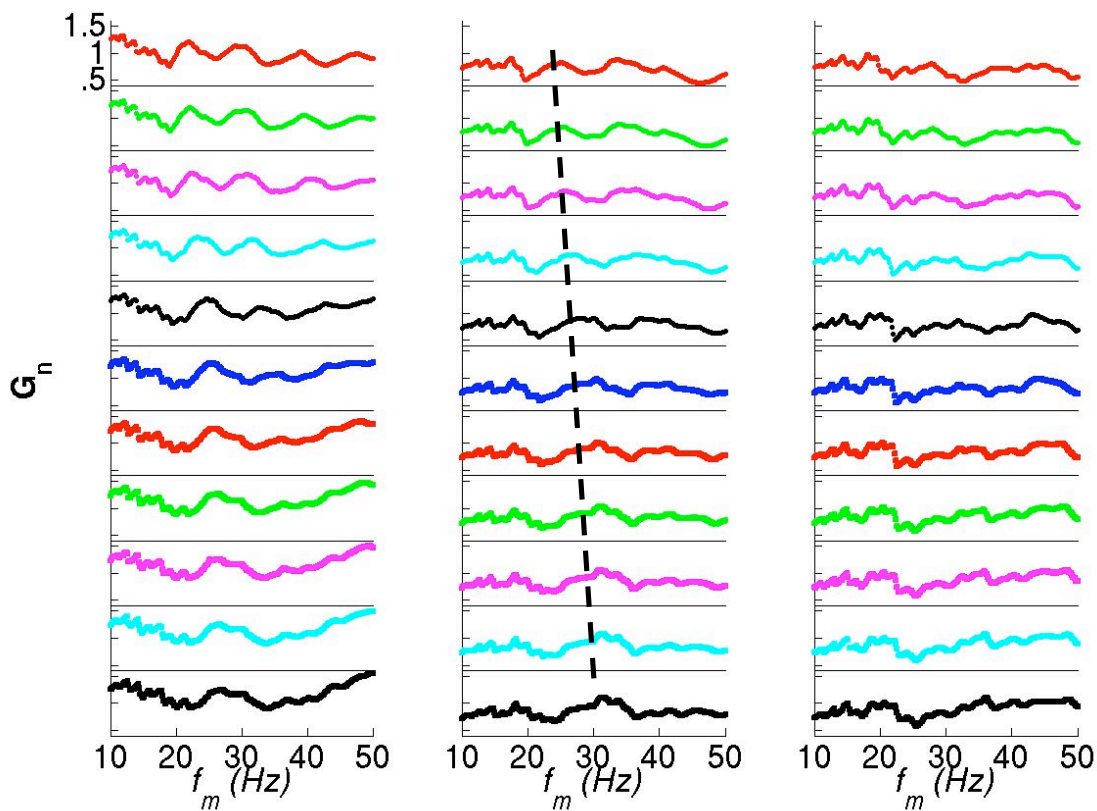

Figure 14 – Receiver/Receiver amplitude ratios, $G_n(R[X+1];R[X])$ for the Z component of receiver pairs (R2;R1), (R3;R2), and (R4;R3) are shown from left to right, respectively. The input voltage increases upwards with the bottom panels showing the amplitude ratios at the lowest input voltage (black) and the top panels showing the amplitude ratios at the highest input voltage (red). The y-axis tick marks are at 0.5, 1.0, and 1.5 as shown in the upper left corner and they are the same for each panel. Dashed black line highlights the shift in peak frequency for R3/R2.
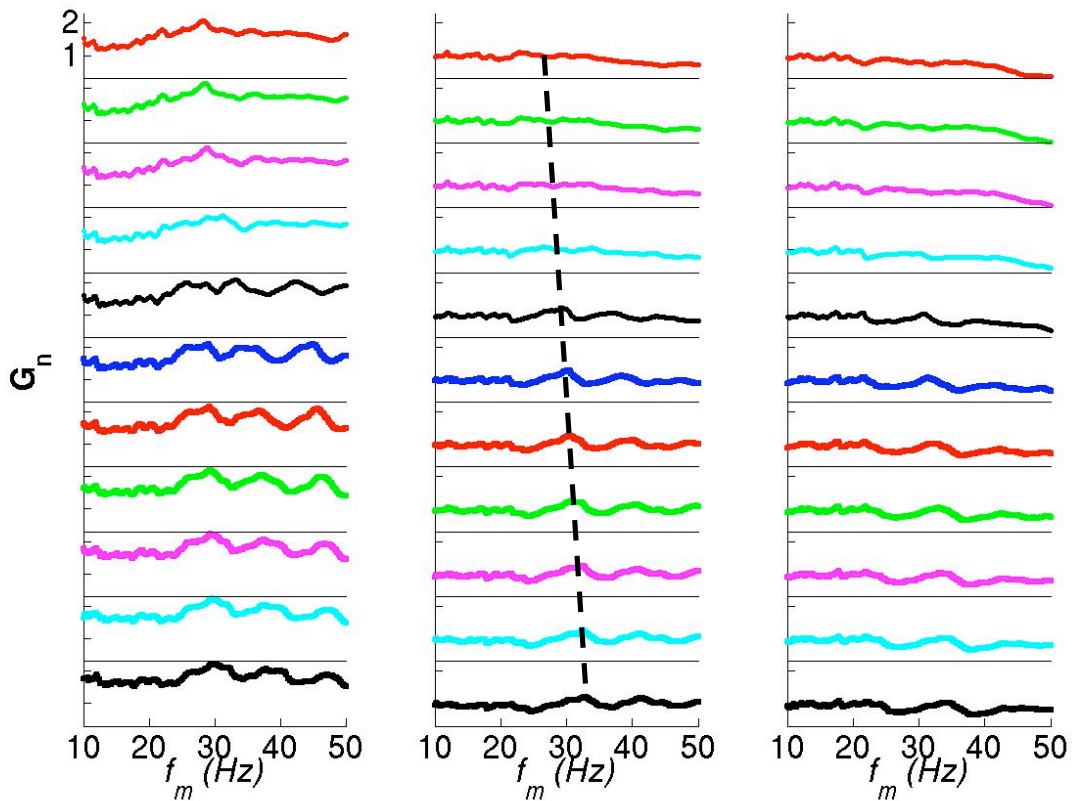
Figure 15 – Receiver/Receiver amplitude ratios, $\mathbf{G}_n$(R[X+1];R[X]) for the N-S component of receiver pairs (R2;R1), (R3;R2), and (R4;R3) are shown from left to right, respectively. The input voltage increases upwards with the bottom panels showing the amplitude ratios at the lowest input voltage (black) and the top panels showing the amplitude ratios at the highest input voltage (red). The y-axis tick marks are at 1.0 and 2.0 as shown in the upper left corner and they are the same for each panel. Dashed black line highlights the shift in peak frequency for R3/R2.
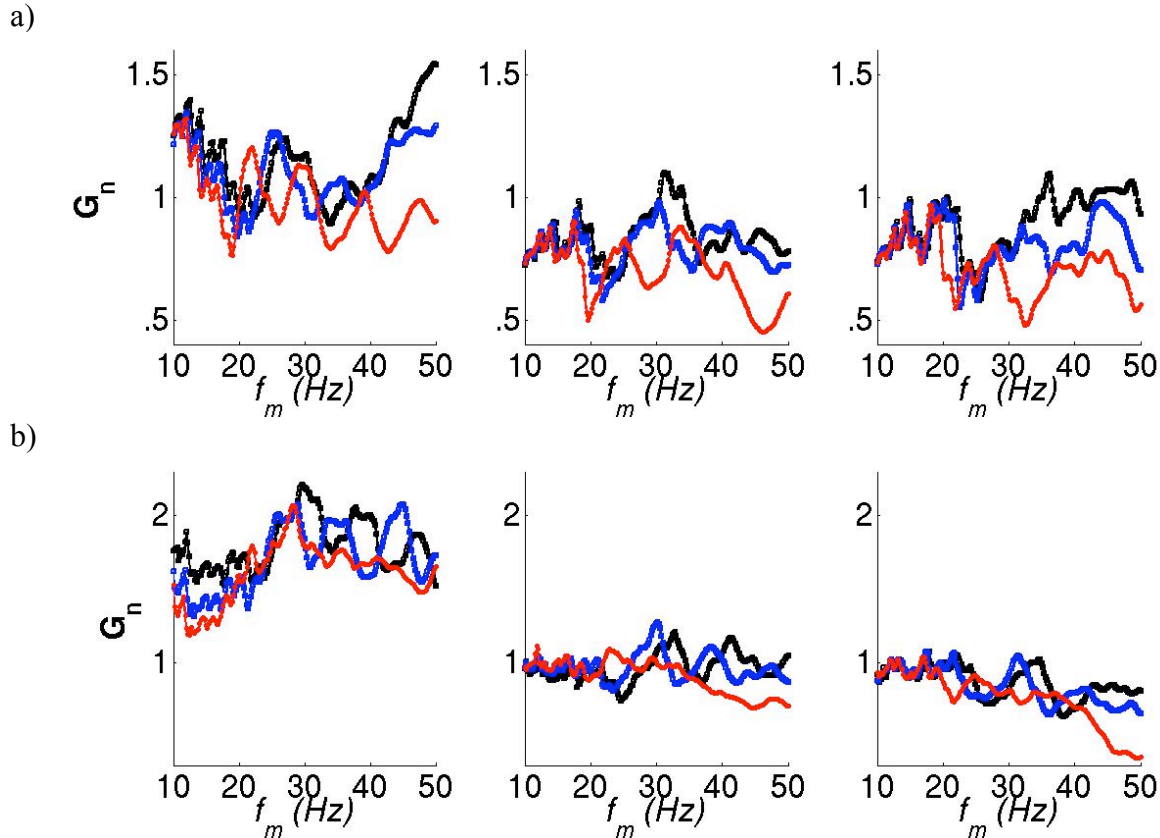
a)

b)

Figure 16 – Receiver/Receiver amplitude ratios for A_1 (black), A_6 (blue), and A_{11} (red). a) Z components and b) N-S components of receivers R1-R4 are shown from left to right, respectively.

6. Discussion

In this study, we observe clear peaks in Receiver/Receiver amplitude ratios that decrease as source amplitude increases. Lawrence et al. [2008] measured phase velocities across a similar type of receiver array using a similar source protocol. They observe systematic decreases in phase velocities between receivers as source amplitude increases. We are currently in the process of extracting phase measurements at steady-state using the homodyne analysis. With steady-state amplitudes and phase velocities for the same experiment, we may better understand the propagation of nonlinear surface waves from vibrator trucks.

Lawrence et al. [2008] inverted the surface wave phase velocities to infer that near surface soils are predominately responsible for the nonlinear soil response. These observations are

consistent with laboratory experiments, which show an inverse relationship between confining pressure and the magnitude of the nonlinear response [Hardin & Drnevich, 1972; Johnson & Jia, 2006]. Qualitatively, the Receiver/Receiver amplitude ratios show more dramatic changes at higher frequencies as the source amplitude increases (see Figure 16), which may be consistent with these observations. Steady-state phase velocity measurements may confirm the depth dependence of the nonlinear soil response observed in this experiment.

Numerical models have been developed that incorporate laboratory derived soil properties into their predictions of nonlinear site response during large earthquakes [Bonilla et al., 2005]. These nonlinear site response models rely on a simple hysteretic soil model such as the extended Masing's rules to describe nonlinear soil response and are limited to scenarios with 1D propagation of shear waves. They do not incorporate more complex phenomena such as harmonic generation and nonlinear surface waves. A primary limitation to developing more rigorous numerical models is the lack of quantitative observations of nonlinear soil response under natural conditions not possible in the laboratory, which we provide in this study.

7. Conclusions

In this study, we describe a novel methodology for studying the *in situ*, nonlinear soil response of a natural soil formation using a vibrator truck and new processing methods. We observe a clear nonlinear soil response in the near field of the vibrator truck using non-invasive measurements at wavelengths and amplitudes similar to those of actual earthquakes. Amplitude ratios between adjacent receivers suggest that the nonlinear soil response extends beyond the source-soil contact region. The magnitude of the nonlinear response we observe appears to be dependent on frequency, and therefore depth, which is consistent with observations from laboratory experiments and the work by Lawrence et al. [2008]. In the future, we plan to test this

method at a site where previous nonlinear site response has been observed and may employ a lower frequency source to achieve frequencies closer to peak frequencies observed during earthquakes. Quantitative observations of nonlinear soil response under natural conditions not possible in the laboratory (i.e. "open" system, seismic wavelengths, depth-dependent soil properties, etc.) provide critical data for testing current models of nonlinear soil response. We hope such observations lead to a better theoretical description of nonlinear soil response that includes surface waves. Ultimately, such advances may lead to the development of inverse methods for extracting nonlinear soil parameters from field-scale measurements like those presented in this study.

8. Conclusions

References

Beresnev, I. A. and K. L. Wen, 1996, Nonlinear soil response – a reality?, *Bull. Seism. Soc. Am.*, *86*, 1964-1978.

Bonilla, L. F., R. J. Archuleta, and D. Lavallee, 2005, Hysteretic and dilatant behavior of cohesionless soils and their effects on nonlinear site response: Field data observations and modeling, *Bull. Seism. Soc. Am.*, *95*, 2373-2395.

Field, E. H., P. A. Johnson, I. Beresnev, and Y. Zeng, 1997, Nonlinear ground-motion amplification by sediments during the 1994 Northridge earthquake, *Nature*, *390*, 599-602.

Field, E. H., Y. Zeng, P. A. Johnson, and I. A. Beresnev, 1998, Pervasive nonlinear response observed during the 1994 Northridge earthquake, *J. Geophys. Res.*, *103*, 26,869-26,883.

Guyer, R. A., and P. A. Johnson, 1999, Nonlinear mesoscopic elasticity: evidence for a new class of materials, *Physics Today*, *52*, 30-35.

Hardin, B. O., 1972, Shear modulus and damping in soils: design equations and curves, *Journal of Soil Mechanics and Foundation Division, 98*, 667-692.

Johnson, P. A., and X. Jia, 2005, Nonlinear dynamics, granular media and dynamic earthquake triggering, *Nature, 437*, 871-874.

Johnson, P. A., B. Zinszner, and P. N. J. Rasolofosaon, 1996, Resonance and nonlinear elastic phenomena in rock, *J. Geophys. Res.-Solid Earth, 101*, 11553-11564.

Kurtulus, A., J. J. Lee, and K. H. Stokoe, 2005, Summary report: site characterization of Capital Aggregates test site, *University of Texas, Austin Internal Report*, 1-47.

Lamb, H., 1904, On the propagation of tremors over the surface of an elastic solid, *Philosophical Transactions of the Royal Society, A203*, 1.

Lawrence, Z., P. Bodin, C.A. Langston, F. Pearce, J. Gomberg, P.A. Johnson, F.Y. Menq, T. Brackman, 2008, Induced dynamic nonlinear ground response at Garner Valley, California, *Bull. Seismo. Soc. Am., 98*, 1412-1428.

Muravskii, G., 2005, On description of hysteretic behaviour of materials, *International Journal of Solids and Structures, 42*, 2625-2644.

Seed, H. B., 1986, Moduli and damping factors for dynamic analyses of cohesionless soils, *Journal of Geotechnical Engineering, 112*, 1016-1032.

Stokoe, K. H., P. J. Axtell, and E. M. Rathje, 2001, Development of an in situ method to measure nonlinear soil behavior, *International Conference on Earthquake Resistant and Engineering Structures III*, 561-570.

Stokoe, K. H., E. M. Rathje, C. R. Wilson, B. L. Rosenblad, and F. Y. Menq, 2004. Development of the NEES large-scale mobile shakers and associated instrumentation for in situ evaluation of nonlinear characteristics and liquefaction resistance of soils, 13th World Conf. on Earthquake Eng., Vancouver, B.C. Canada, August 1–6, Paper No. 535, 10 pp.

Williams, R. A., W. J. Stephenson, A. D. Frankel, E. Cranswick, M. E. Meremonte, and J. K. Odum, 2000, Correlation of 1- to 10-Hz earthquake resonances with surface measurements of S-wave reflections and refractions in the upper 50-m, *Bull. Seism. Soc. Am., 90*, 1323-1331.